
VOXURF: VOXEL-BASED EFFICIENT AND ACCURATE NEURAL SURFACE RECONSTRUCTION

Tong Wu^{1,2}, Jiaqi Wang², Xingang Pan³, Xudong Xu¹, Christian Theobalt³, Ziwei Liu⁴, Dahua Lin^{1,2,5}

¹SenseTime-CUHK Joint Lab, The Chinese University of Hong Kong,

²Shanghai AI Laboratory, ³Max Planck Institute for Informatics,

⁴S-Lab, Nanyang Technological University, ⁵Centre of Perceptual and Interactive Intelligence

{wt020, xx018, dhlin}@ie.cuhk.edu.hk, wangjiaqi@pjlab.org.cn,

{xpan,theobalt}@mpi-inf.mpg.de, ziwei.liu@ntu.edu.sg

ABSTRACT

Neural surface reconstruction aims to reconstruct accurate 3D surfaces based on multi-view images. Previous methods based on neural volume rendering mostly train a fully implicit model with MLPs, which typically require hours of training for a single scene. Recent efforts explore the explicit volumetric representation to accelerate the optimization via memorizing significant information with learnable voxel grids. However, existing voxel-based methods often struggle in reconstructing fine-grained geometry, even when combined with an SDF-based volume rendering scheme. We reveal that this is because 1) the voxel grids tend to break the color-geometry dependency that facilitates fine-geometry learning, and 2) the under-constrained voxel grids lack spatial coherence and are vulnerable to local minima. In this work, we present **Voxurf**, a voxel-based surface reconstruction approach that is both efficient and accurate. Voxurf addresses the aforementioned issues via several key designs, including 1) a two-stage training procedure that attains a coherent coarse shape and recovers fine details successively, 2) a *dual color network* that maintains color-geometry dependency, and 3) a *hierarchical geometry feature* to encourage information propagation across voxels. Extensive experiments show that Voxurf achieves high efficiency and high quality at the same time. On the DTU benchmark, Voxurf achieves higher reconstruction quality with a 20x training speedup compared to previous fully implicit methods. Our code will be made publicly available.

1 INTRODUCTION

Neural surface reconstruction based on multi-view images has recently seen dramatic progress. Inspired by the success of Neural Radiance Fields (NeRF) (Mildenhall et al., 2020) on Novel View Synthesis (NVS), recent works follow the neural volume rendering scheme to represent the 3D geometry with a signed distance function (SDF) or occupancy field via a fully implicit model (Oechsle et al., 2021; Yariv et al., 2021; Wang et al., 2021). These approaches train a deep multilayer perceptron (MLP), which takes in hundreds of sampled points on each camera ray and outputs the corresponding color and geometry information. Pixel-wise supervision is then applied by measuring the difference between the accumulated color on each ray and the ground truth. Struggling with learning all the geometric and color details with a pure MLP-based framework, these methods require hours of training for a single scene, which substantially limits their real-world applications.

Recent advances in NeRF accelerate the training process with the aid of an explicit volumetric representation (Sun et al., 2021; Yu et al., 2021; Chen et al., 2022). These works directly store and optimize the geometry and color information via explicit voxel grids. For example, the density of a queried point can be readily interpolated from the eight neighboring points, and the view-dependent color is either represented with spherical harmonic coefficients (Yu et al., 2021) or predicted by shallow MLPs that take learnable grid features as auxiliary inputs (Sun et al., 2021). These approaches achieve competitive rendering performance at a much lower training cost (< 20 minutes). However, their 3D surface reconstruction results cannot faithfully represent the exact geometry, suffering from

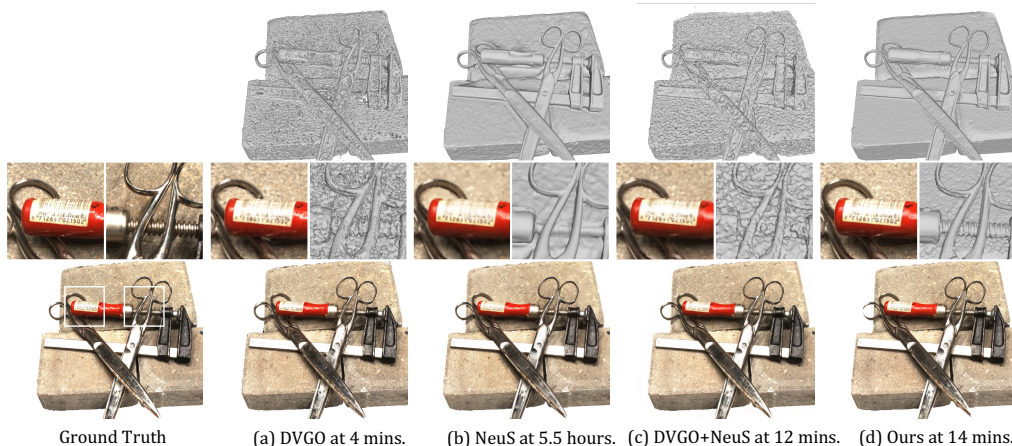


Figure 1: **Comparisons among different methods for surface reconstruction and novel view synthesis.** (a) DVGO (v2) (Sun et al., 2021; 2022) benefits from the fastest convergence but suffers from a poor surface reconstruction; (b) NeuS (Wang et al., 2021) produces decent surfaces after a long training time, while high-frequency details are lost in both the geometry and the image; (c) the straightforward combination of DVGO and NeuS produces continuous but noisy surfaces; (d) our method achieves around 20x speedup than NeuS and recovers high-quality surfaces and images with fine details. All the training times are tested on a single Nvidia A100 GPU.

conspicuous noise and holes (Fig. 1 (a)). It is due to the inherent ambiguity of the density-based volume rendering scheme, and the explicit volumetric representation introduces additional challenges.

In this work, we aim to take advantage of the explicit volumetric representation for efficient training and propose customized designs to harvest high-quality surface reconstruction. A straightforward idea for this purpose is to embed the SDF-based volume rendering scheme (Wang et al., 2021; Yariv et al., 2021) into explicit volumetric representation frameworks (Sun et al., 2021). However, we find this naïve baseline model not working well by losing most of the geometry details and producing undesired noise (Fig. 1 (c)). We reveal several critical issues for this framework as follows. First, in fully implicit models, the color network takes surface normals as inputs, effectively building *color-geometry dependency* that facilitates fine-geometry learning. However, in the baseline model, the color network tends to depend more on the additional under-constraint voxel feature grid input, thus breaking color-geometry dependency. Second, due to a high degree of freedom in optimizing a voxel grid, it is hard to maintain a globally coherent shape without additional constraints. Individual optimization for each voxel point hinders the information sharing across the voxel grid, which hurts the surface smoothness and introduces local minima. We’ll unveil these effects and introduce the insight for our architecture design via an empirical study in Sec. 4

To tackle the challenges, we introduce **Voxurf**, an efficient pipeline for accurate **Voxel-based surface reconstruction**: 1) We leverage a two-stage training process that attains a coherent coarse shape and recovers fine details successively. 2) We design a *dual color network* that is capable of representing a complex color field via a voxel grid and preserving the color-geometry dependency with two sub-networks that work in synergy. 3) We also propose a *hierarchical geometry feature* based on the SDF voxel grid to encourage information sharing in a larger region for stable optimization. 4) We introduce several effective regularization terms to boost smoothness and reduce noise.

We conduct experiments on the DTU (Jensen et al., 2014) and BlendedMVS (Yao et al., 2020) datasets for quantitative and qualitative evaluations. Experimental results demonstrate that Voxurf achieves lower Chamfer Distance on the DTU (Jensen et al., 2014) benchmark than a competitive fully implicit method NeuS (Wang et al., 2021) with around 20x speedup. It also achieves remarkable results on the auxiliary task of NVS. As illustrated in Fig. 1, our method is shown to be superior in preserving high-frequency details in both geometry reconstruction and image rendering compared to the previous approaches. In summary, our contributions are highlighted below:

1. Our approach enables around 20x speedup for training compared to the SOTA methods, reducing the training time from over 5 hours to 14 minutes on a single Nvidia A100 GPU.

2. Our approach achieves higher surface reconstruction fidelity and novel view synthesis quality, which is superior in representing fine details for both surface recovery and image rendering compared to previous methods.
3. Our study provides insightful observations and analysis of the architecture design of the explicit volumetric representation framework for surface reconstruction.

2 RELATED WORKS

Multi-view 3D reconstruction Recently, implicit representations that encode the geometry and appearance of a 3D scene by neural networks have gained a lot of attention (Park et al., 2019; Chen & Zhang, 2019; Lombardi et al., 2019; Mescheder et al., 2019; Sitzmann et al., 2019; Saito et al., 2019; Atzmon et al., 2019; Jiang et al., 2020; Zhang et al., 2021; Toussaint et al., 2022). Among them, a plethora of papers have explored neural surface reconstruction from multi-view images. Methods based on surface rendering (Niemeyer et al., 2020; Yariv et al., 2020; Liu et al., 2020; Kellnhofer et al., 2021) regard the color of an intersection point of the ray and the surface as the final rendered color. However, they usually require accurate object masks and careful weight initialization. To get rid of the mask requirement, recent approaches (Wang et al., 2021; Yariv et al., 2021; Oechsle et al., 2021; Darmon et al., 2021) based on volume rendering (Max, 1995) formulate the radiance fields and implicit surface representations in a unified model, thereby achieving the merits of both techniques. However, encoding the whole scene in pure MLP networks requires a long training time. In a departure from these works, we leverage learnable voxel grids and shallow color networks for quick convergence, as well as pursue more fine details in surfaces and rendered images.

Explicit volumetric representation Despite the great success of implicit neural representations in 3D modeling, recent advances have integrated explicit 3D representations, *e.g.*, point clouds, voxels, and MPIS (Mildenhall et al., 2019), and received growing attention (Wizadwongsa et al., 2021; Xu et al., 2022; Lombardi et al., 2019; Wang et al., 2022; Fang et al., 2022). Instant-ngp (Müller et al., 2022) uses multi-resolution hashing for efficient encoding and implements fully-fused CUDA kernels for fast convergence. Plenoxels (Yu et al., 2021) represent a scene as a sparse 3D grid with spherical harmonics and are optimized two orders of magnitude faster than NeRF (Mildenhall et al., 2020) with competitive visual quality. TensorRF (Chen et al., 2022) considers the full volume field as a 4D tensor and factorizes it into multiple compact low-rank tensor components for efficient modeling. The method most related to ours is DVGO (Sun et al., 2021), which adopts a hybrid architecture design including voxel grids and a shallow MLP. Despite their remarkable results on novel view synthesis, none of them is designed to faithfully reconstruct the geometry of the scene. In contrast, we target at not only rendering photo-realistic images from novel viewpoints but also reconstructing high-quality surfaces with fine details.

3 PRELIMINARIES

Volume rendering with SDF representation. NeuS (Wang et al., 2021) represents a scene as an implicit SDF field parameterized by an MLP. The ray emitting from the camera center o through an image pixel in the viewing direction v can be expressed as $\{p(t) = o + tv | t \geq 0\}$. The rendered color for the image pixel is integrated along the ray with volume rendering (Max, 1995), which is approximated by N discrete sampled points $\{p_i = o + t_i v | i = 1, \dots, N, t_i < t_{i+1}\}$ on the ray:

$$\hat{C}(r) = \sum_{i=1}^N T_i \alpha_i c_i, \quad T_i = \prod_{j=1}^{i-1} (1 - \alpha_j), \quad (1)$$

where α_i is the opacity value, and T_i is the accumulated transmittance. The key difference between NeuS and NeRF is the formula of α_i . In NeuS, α_i is formulated as:

$$\alpha_i = \max \left(\frac{\Phi_s(f(p(t_i))) - \Phi_s(f(p(t_{i+1})))}{\Phi_s(f(p(t_i)))}, 0 \right). \quad (2)$$

Here, $f(x)$ is the SDF function, and $\Phi_s(x) = (1 + e^{-sx})^{-1}$ is the Sigmoid function, where the s value is learned or manually updated during training.

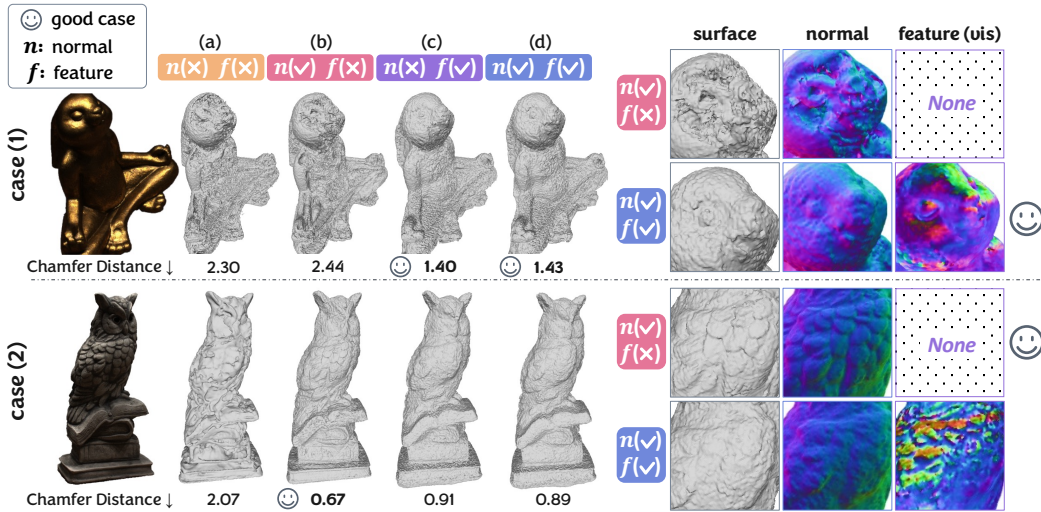


Figure 2: **Reconstruction results from different architecture designs.** The *surface normal* n and *learnable feature* f are both optional inputs to the color network. We show results of two cases under four settings on the **left**, and we zoom in to analyze the surfaces, normal fields, and feature fields on the **right**. Case (1) (a, c) and (b, d) show that the feature f helps maintain a coherent shape, while case (2) (b, d) reveal that it discourages the reconstruction of geometry details since it disturbs the color-geometry dependency built by the normal n .

Explicit volumetric representation. DVGO (Sun et al., 2021) proposes to represent the geometry with explicit density voxel grids $V^{(density)} \in \mathbb{R}^{1 \times N_x \times N_y \times N_z}$. It applies a hybrid architecture for color prediction that comprises a shallow MLP parameterized by Θ and a feature voxel grid $V^{(feat)} \in \mathbb{R}^{C \times N_x \times N_y \times N_z}$. Given a 3D position p and the viewing direction v , the volume density σ and color c are estimated with:

$$\sigma = \text{interp}(p, V^{(density)}), \quad (3)$$

$$c = \text{MLP}_{\Theta}(\text{interp}(p, V^{(feat)}), p, v), \quad (4)$$

where ‘interp’ denotes the trilinear interpolation. Following NeRF (Mildenhall et al., 2020; Tancik et al., 2020), the positional encoding for both p and v is applied in Eqn. 4.

Naïve Combination. A straightforward combination of the two techniques is to replace the volume rendering in DVGO with the SDF-based volume rendering scheme as in Eqn. 1 and Eqn. 2. It serves as the naïve baseline in this work, which can hardly produce satisfactory results, as shown in Fig. 1 (c). We will cast light on this phenomenon via an empirical study in the next section.

4 STUDY ON ARCHITECTURE DESIGN FOR GEOMETRY LEARNING

In this section, we carry out some prior experiments with variants of the baseline model, aiming to figure out the key factors for architecture design in this task. Specifically, we employ an SDF voxel grid $V^{(sdf)}$ and apply Eqn. 2 for α calculation with a manually defined schedule for s . We start with a shallow MLP as the color network, where 1) the local feature f interpolated from $V^{(feat)}$ and 2) the normal vector n calculated by $V^{(sdf)}$ are both optional inputs. A decent surface reconstruction is expected to possess *a coherent coarse structure*, *accurate fine details*, and *a smooth surface*. We will next focus on these factors and analyze the effects of different architecture designs.

The key to maintaining a coherent coarse shape. Intuitively, the capacity of a shallow MLP is limited, and it can hardly represent a complex scene with different materials, high-frequency textures, and view-dependent lighting information. When the ground truth image encounters a rapid color-shifting, the volume rendering integration over an under-fitted color field results in a corrupted geometry, as shown in Fig. 2 case (1) (a) and (b). Incorporating the local feature f enables fast color learning and increases the representation ability of the network, and the problem is noticeably alleviated, as shown in Fig. 2 case (1), the differences between (a) and (c), (b) and (d).

The key to reconstructing accurate geometry details. We then introduce another case in Fig. 2 case (2). Its texture changes moderately, and the color is largely correlated with the surface normal

due to diffuse reflection. Although the geometry still collapses given neither normal n or feature f as input in Fig. 2 case (2) (a), we can observe a reasonable reconstruction even with some geometry details in Fig. 2 case (2) (b) with only n as the input. Incorporating the feature f does not further reduce the Chamfer Distance (CD); instead, geometry details are missing since the learnable feature f disturbs the geometry-color dependency, *i.e.*, the relationship built between the color and the surface normal, as shown in Fig. 2 case (2), the differences between (b) and (d).

The reason for noisy surfaces. For all the cases above, the results suffer from obvious noise on the surface. Compared with learning an implicit representation globally, the under-constrained voxel grids lack spatial coherence and are vulnerable to local minima, which hurts the continuity and smoothness of the surface.

These observations motivate us to design the network architecture, training scheme, and losses in our method that can facilitate fine-geometry learning.

5 METHODOLOGY

Inspired by the insight revealed in Sec. 4, we propose several key designs: 1) we adopt a two-stage training procedure that attains a coherent coarse shape (Sec. 5.1) and recovers fine details (Sec. 5.2) successively; 2) we propose a dual color network to maintain color-geometry dependency and recover precise surfaces and novel-view images; 3) we design a hierarchical geometry feature to encourage information propagation across voxels for stable optimization; 4) we also introduce smoothness priors, including a gradient smoothness loss for better visual quality (Sec. 5.3).

5.1 COARSE SHAPE INITIALIZATION

We initialize our SDF voxel grid $V^{(sdf)}$ with an ellipsoid-like zero level set inside a prepared region for reconstruction as in (Sun et al., 2021). We then perform coarse shape optimization with the aid of $V^{(feat)}$ as introduced in Sec. 4. Specifically, we train a shallow MLP with both normal vector n and local feature f as inputs, along with the embedded position p and viewing direction v . To encourage a stable training process and smooth surface, we propose to conduct the interpolation on a smoothed voxel grid rather than the raw data of $V^{(sdf)}$. In particular, we denote $\mathcal{G}(V, k_g, \sigma_g)$ as applying 3D convolution on the voxel grid V with a Gaussian kernel, whose weight matrix follows a Gaussian distribution: $K_{i,j,k} = 1/Z \times \exp(-((i - \lfloor k_g/2 \rfloor)^2 + (j - \lfloor k_g/2 \rfloor)^2 + (k - \lfloor k_g/2 \rfloor)^2)/2\sigma_g^2)$, $i, j, k \in \{0, 1, \dots, k_g - 1\}$, where Z denotes a normalization term, k_g denotes the kernel size, and σ_g denotes the standard deviation. Querying a smoothed SDF value d' of an arbitrary point p thus becomes:

$$d' = \text{interp}(p, \mathcal{G}(V^{(sdf)}, k_g, \sigma_g)). \quad (5)$$

We use d' for the ray marching integration following Eqn. 1 and Eqn. 2 and calculate the reconstruction loss. We also apply several smoothness priors as to be introduced in Sec. 5.3

5.2 FINE GEOMETRY OPTIMIZATION

At this stage, we aim to recover accurate geometry details based on the coarse initialization. We note that the challenges are two-fold: **1)** The study in Sec. 4 reveals a trade-off introduced by the feature voxel grid, *i.e.*, the representation capacity of the color field is improved at the sacrifice of color-geometry dependency. **2)** The optimization of the SDF voxel grid is based on trilinear interpolation to query a 3D point. The operation brings in fast convergence, while it also limits information sharing across different locations, which may lead to local minima with degenerate solutions and a sub-optimal smoothness. We propose a *dual color network* and a *hierarchical geometry feature* to address these two issues, respectively.

Dual color network. The observation in Sec. 4 encourages us to design a dual color network that takes advantage of the local feature f_i^{feat} interpolated from the learnable feature voxel grid $V^{(feat)}$ without losing the color-geometry dependency. As shown in Fig. 3, we train two shallow MLPs with different additional inputs besides the embedded position and view direction. The first MLP g_{geo} takes the hierarchical geometry feature f_i^{geo} , which will be introduced later, to build the color-geometry dependency; the second one g_{feat} takes both a simple geometry feature (*i.e.*, the surface normal n_i) and the local feature f_i^{feat} as inputs to enable a faster and more precise color learning,

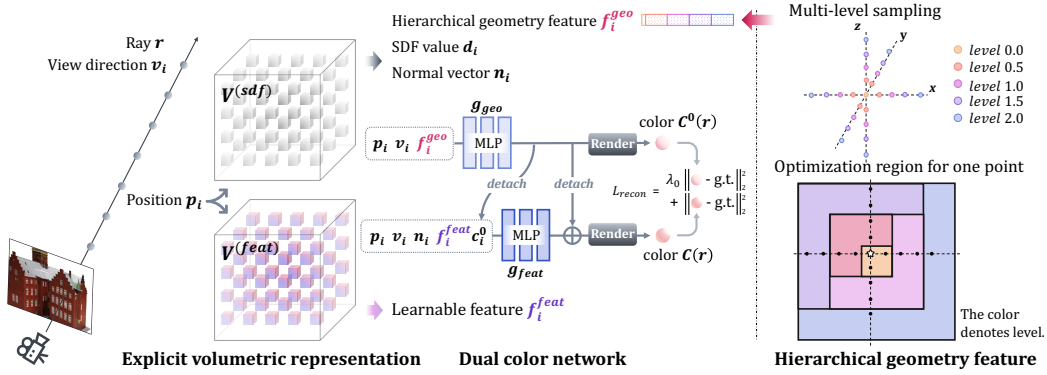


Figure 3: **Overview of key components in our model.** We adopt an explicit volumetric representation with an SDF voxel grid $V^{(sdf)}$ and a feature voxel grid $V^{(feat)}$. In the middle, we show the design for our dual color network, where f_i^{feat} is the interpolated feature from $V^{(feat)}$ at point p_i , and f_i^{geo} denotes the hierarchical feature constructed on the right. Here we show the multi-level sampling scheme and the region of grids that is affected by one point during optimization with different settings of levels.

which will in turn benefit the geometry optimization. The two networks are combined in a residual manner with detaching operations: the output of g_{geo} , denoted by c_0 , is detached before input to g_{feat} , and the output is added back to a detached copy of c_0 to get the final color prediction c .

Outputs of both g_{geo} and g_{feat} are supervised by a reconstruction loss between the ground truth image and the integrated color along the ray. Specifically, the rendered colors from them are denoted as $C^0(r)$ and $C(r)$, and the overall reconstruction loss is formulated as:

$$\mathcal{L}_{recon} = \frac{1}{\mathcal{R}} \sum_{r \in \mathcal{R}} \left(\|C(r) - \hat{C}(r)\|_2^2 + \lambda_0 \|C_0(r) - \hat{C}(r)\|_2^2 \right), \quad (6)$$

where $\hat{C}(r)$ denotes the ground truth color, and λ_0 denotes a loss weight. $V^{(feat)}$ and the MLP g_{feat} fit the scene field rapidly, while the MLP g_{geo} fits the scene at a relatively slower pace. The detaching operations promote a stable optimization of g_{geo} guided by the reconstruction loss of itself, which helps preserve color-geometry dependency.

Hierarchical geometry feature. Using the surface normal n as the geometry feature for the color networks is a straightforward choice, while it takes in information only from adjacent grids of $V^{(SDF)}$. In order to enlarge the perception area and encourage information propagation across voxels, we propose to look at a larger region of the SDF field and take the corresponding SDF values and gradients as an auxiliary condition to the color networks. Specifically, for a given 3D position $p = (x, y, z)$, we take half of the voxel size v_s as the step size and define its neighbours along the X, Y, Z axis on both sides. Taking the X axis as an example, the neighbouring coordinates are defined as $p_x^{l-} = (x^{l-}, y, z)$ and $p_x^{l+} = (x^{l+}, y, z)$, where $x^{l-} = \max(x - l * v_s, 0)$, $x^{l+} = \min(x + l * v_s, v_x^m)$, $l \in [0.5, 1.0, 1.5, \dots]$ denotes the ‘level’ of neighbour area, and v_x^m denotes the maximum of the voxel grid on x axis. We then extend the definition to a hierarchical manner by concatenating the neighbours from different levels together as formulated below:

$$d_k^l = [d_k^{l-}, d_k^{l+}] = [\text{interp}(p_k^{l-}, V^{(sdf)}), \text{interp}(p_k^{l+}, V^{(sdf)})], k \in \{x, y, z\}, \quad (7)$$

$$f_p^{sdf}(l) = [d^0, d_x^{0.5}, d_y^{0.5}, d_z^{0.5}, \dots, d_x^l, d_y^l, d_z^l]^T,$$

where d_x^l denotes the SDF values queried from $V^{(sdf)}$ at locations p_x^{l-} and p_x^{l+} . When $l = 0$, $f_p^{sdf}(0) = d^0$, which is exactly the SDF value at the location p itself. Then, we also incorporate the gradient information into the geometry feature. Specifically, we can gain the gradient vector $\delta_x^l = (d_x^{l+} - d_x^{l-}) / (2 * l * v_s)$, and the approximate normal vector $n^l \in \mathbb{R}^3$ is to normalize the $[\delta_x^l, \delta_y^l, \delta_z^l]$ to a L2-norm of 1. The hierarchical version of the normal is formulated as:

$$f_p^{normal}(l) = [n^{0.5}, \dots, n^l]. \quad (8)$$

Finally, the hierarchical geometry feature at point p for a predefined level $l \in [0.5, 1.0, 1.5, \dots]$ is to combine the information above by:

$$f_p^{geo}(l) = [f_p^{sdf}(l), f_p^{normal}(l)]. \quad (9)$$

As shown in Fig. 3, $f_p^{geo}(l)$ is input to the MLP g_{geo} to assist geometry learning.

Table 1: Quantitative evaluation on DTU dataset.

| Scan | 24 | 37 | 40 | 55 | 63 | 65 | 69 | 83 | 97 | 105 | 106 | 110 | 114 | 118 | 122 | mean |
|-------------------------------|-------------|-------------|-------------|-------------|-------------|-------------|-------------|-------------|-------------|-------------|-------------|-------------|-------------|-------------|-------------|-------------|
| NeRF(Mildenhall et al., 2020) | 1.83 | 2.39 | 1.79 | 0.66 | 1.79 | 1.44 | 1.50 | 1.20 | 1.96 | 1.27 | 1.44 | 2.61 | 1.04 | 1.13 | 0.99 | 1.54 |
| IDR(Yariv et al., 2020) | 1.63 | 1.87 | 0.63 | 0.48 | 1.04 | 0.79 | 0.77 | 1.33 | 1.16 | 0.76 | 0.67 | 0.90 | 0.42 | 0.51 | 0.53 | 0.90 |
| DVGO(Sun et al., 2021) | 1.83 | 1.74 | 1.70 | 1.53 | 1.91 | 1.91 | 1.77 | 2.60 | 2.08 | 1.79 | 1.76 | 2.12 | 1.60 | 1.80 | 1.58 | 1.85 |
| NeuS(Wang et al., 2021) | 0.83 | 0.98 | 0.56 | 0.37 | 1.13 | 0.59 | 0.60 | 1.45 | 0.95 | 0.78 | 0.52 | 1.43 | 0.36 | 0.45 | 0.45 | 0.77 |
| DVGO + NeuS | 1.24 | 0.87 | 0.74 | 0.48 | 1.20 | 1.41 | 1.113 | 1.96 | 1.44 | 0.98 | 1.13 | 1.99 | 1.62 | 0.77 | 0.62 | 1.13 |
| Ours | 0.65 | 0.74 | 0.39 | 0.35 | 0.96 | 0.64 | 0.85 | 1.58 | 1.01 | 0.68 | 0.60 | 1.11 | 0.37 | 0.45 | 0.47 | 0.72 |

Table 2: An overall comparison on surface reconstruction, novel view synthesis, and training time on DTU.

| | PSNR \uparrow | SSIM \uparrow | LPIPS \downarrow | CD \downarrow | Time (Nvidia A100) |
|--------------------------|-----------------|-----------------|--------------------|-----------------|--------------------|
| DVGO (Sun et al., 2021) | 31.64 | 0.916 | 0.159 | 1.85 | 4 mins |
| NeuS (Wang et al., 2021) | 29.63 | 0.892 | 0.199 | 0.77 | 5.5 hours |
| Ours | 32.16 | 0.929 | 0.144 | 0.72 | 14 mins |

5.3 SMOOTHNESS PRIORS

We incorporate several effective regularization terms to facilitate surface smoothness during training.

(1) First, we adopt a total variation (TV) regularization (Rudin & Osher, 1994):

$$\mathcal{L}_{TV}(V) = \sum_{d \in [D]} \sqrt{\Delta_x^2(V, d) + \Delta_y^2(V, d) + \Delta_z^2(V, d)}, \quad (10)$$

where $\Delta_x^2(V, d)$ denotes the squared difference between the value of d th channel in voxel $v := (i; j; k)$ and the d th value in voxel $(i + 1; j; k)$, which can be analogously extended to $\Delta_y^2(V, d)$ and $\Delta_z^2(V, d)$. We apply the TV term above to the SDF voxel grid, denoted by $\mathcal{L}_{TV}(V^{(sdf)})$, which encourages a continuous and compact geometry.

(2) We also assume the surface to be smooth in a local area, and we follow the definition of the Gaussian convolution in Sec. 5.1 and introduce a smoothness regularization formulated as:

$$\mathcal{L}_{smooth}(V) = \|\mathcal{G}(V, k_g, \sigma_g) - V\|_2^2, \quad (11)$$

We apply the smoothness term above to the gradient of SDF voxel grid for a *gradient smoothness loss*, denoted by $\mathcal{L}_{smooth}(\nabla V^{(sdf)})$. It encourages a smooth surface and alleviates the issue of noisy points in the free space. Notice that we can also naturally conduct post-processing on the SDF field after training, thanks to its explicit representation. For example, applying the Gaussian kernel above before extracting the geometry can further boost surface smoothness for better visualization.

Finally, the overall training loss is formulated as:

$$\mathcal{L} = \mathcal{L}_{recon} + \lambda_{tv} \mathcal{L}_{TV}(V^{(sdf)}) + \lambda_s \mathcal{L}_{smooth}(\nabla V^{(sdf)}), \quad (12)$$

where λ_{tv} and λ_s denote the weights for the corresponding loss terms.

6 EXPERIMENTS

Experimental setup. We use the DTU (Jensen et al., 2014) dataset for quantitative and qualitative comparisons and show qualitative results on several challenging scenes from the BlendedMVS (Yao et al., 2020) dataset. We include several baselines for comparisons: 1) IDR (Yariv et al., 2020), 2) NeuS (Wang et al., 2021), 3) NeRF (Mildenhall et al., 2020), 4) DVGO (Sun et al., 2021). The results of 1), 2), and 3) are taken from the original papers (Yariv et al., 2020; Wang et al., 2021), and all the methods are reported in the setting with a clean background for a fair comparison. Experimental results with non-empty backgrounds and comparisons with more methods (Schönberger et al., 2016; Oechsle et al., 2021; Yariv et al., 2021) are included in the supplementary materials. Please also refer to the supplementary materials for further descriptions of the datasets, baseline methods, and implementation details.

6.1 COMPARISONS

The quantitative results for surface reconstruction on DTU are reported in Table 1. Quantitative experimental results show that we achieve lower Chamfer Distances than previous methods under

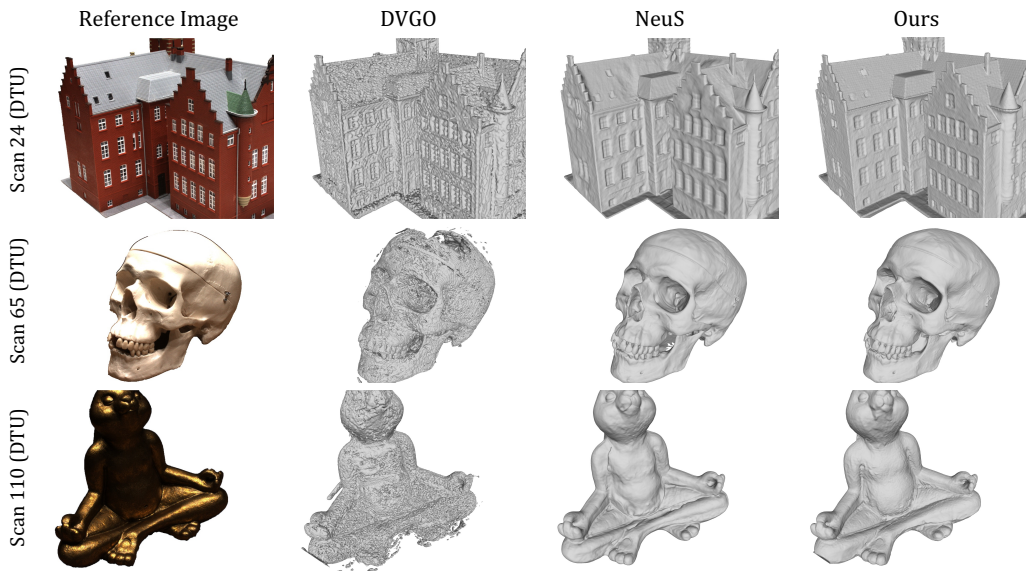


Figure 4: Qualitative comparisons on the DTU dataset. See more scenes in supplementary materials.

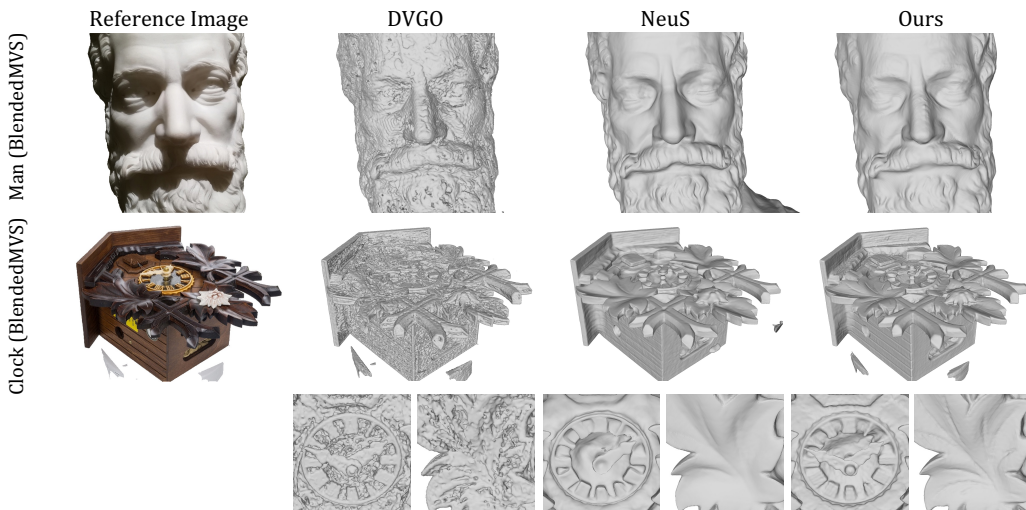


Figure 5: Qualitative comparisons on the BlendedMVS dataset. See more scenes in supplementary materials.

the same setting. We conduct qualitative comparisons on both DTU and BlendedMVS in Fig. 4 and Fig. 5, respectively. DVGO shows poor reconstruction quality with noise and holes since it is designed for novel view synthesis rather than surface reconstruction. NeuS and ours show accurate and continuous surface recovery in a variety of cases. In comparison, NeuS, as a fully implicit model, naturally benefits from the intrinsic continuity and encourages smoothness in local areas, while it sometimes fails to recover very thin geometry details due to over-smoothing. In contrast, our method is superior in recovering fine geometry details thanks to our designs in Sec. 5.

We further perform a more extensive evaluation of our method on surface reconstruction, novel view synthesis, and training time in Table 2. Our method outperforms DVGO and NeuS on both surface reconstruction and novel view synthesis by a clear margin on all the metrics. Notably, our method achieves around **20x** speedup compared to NeuS for producing high-quality surface reconstruction.

6.2 ANALYSIS

In this section, we carry out a series of ablation studies to evaluate each technical component.

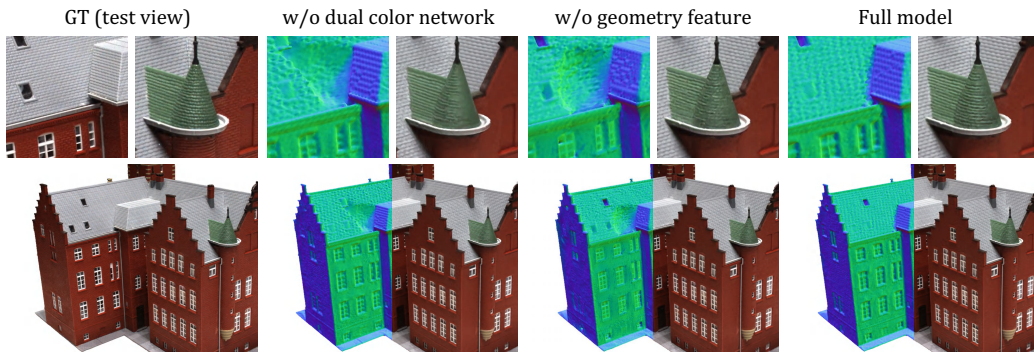


Figure 6: The dual color network learns the color field for complex scenes well and preserves color-geometry dependency, which facilitates geometry learning (see the roofs); the hierarchical geometry feature promotes accurate surface reconstruction (see the windows).

Table 3: Ablation over the effect of dual color network and hierarchical geometry feature.

| CD | 0.91 | 0.79 | 0.77 | 0.72 |
|--------------|------|------|------|-------------|
| Dual | | ✓ | | ✓ |
| Hierarchical | | | ✓ | ✓ |

Table 4: Ablation over the *Residual* and *Detach* designs of the dual color network (Sec. 5.2).

| CD | 0.77 | 0.75 | 0.75 | 0.72 |
|----------|------|------|------|-------------|
| Residual | | ✓ | | ✓ |
| Detach | | | ✓ | ✓ |

The effect of the dual color network and a hierarchical geometry feature. As shown in Table 3, both techniques individually work well on the baseline model, and a combination of them produces the best result. 1) The effect of dual color network can be directly sensed in the improvement of image rendering quality, as can be seen from the comparison of roof textures in Fig. 6. An accurate color field and the color-geometry dependency will promote geometry learning, as can be observed from the comparison of roof geometries (viewed in normal images) in Fig. 6. Experimental results in Table 4 also validate the effectiveness of the design introduced in Sec. 5.2, including the residual color and detachment. 2) Hierarchical geometry feature directly promotes an accurate surface reconstruction, as demonstrated by results in Table 3 and the difference between normal images of Fig. 6. We also explore different design details, including the level selection and the effects of gradient and SDF value in supplementary materials.

Ablation over smoothness priors. We make efforts to encourage the continuity and smoothness of the reconstructed surface at different stages. As shown in Fig. 7 (a), during the coarse shape initialization stage, the naive solution produces holes and noises. Applying the Gaussian convolution substantially alleviates the problem and leads to a more compact geometry. Regularization terms including the TV and our gradient smoothness loss would further encourage a clean and smooth surface to provide a good initialization for the next stage. Fig. 7 (b) shows that during the fine geometry optimization stage, the regularization terms also help maintain surface smoothness. Finally, as shown in Fig. 7 (c), post processing on a trained model can promote surface smoothness for a better visualization quality and maintain an accurate structure at the same time. An ablation study on the effects of the SDF TV term and our gradient smoothness loss is in the supplementary materials.

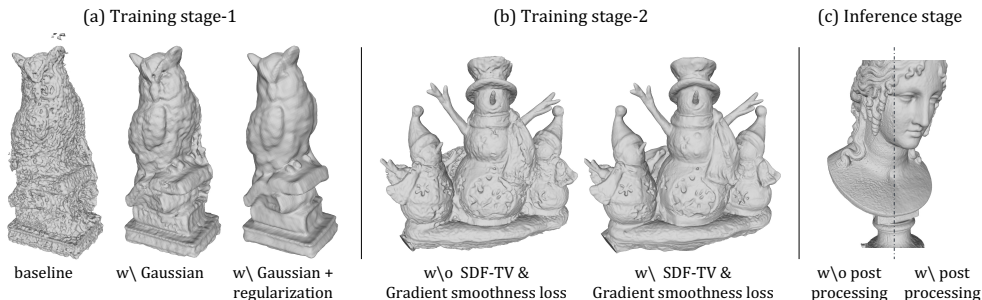


Figure 7: Studies on technical components that encourage surface smoothness during the (a) coarse shape initialization, (b) fine geometry optimization, and (c) post-processing stage.

7 CONCLUSION

This paper proposes **Voxurf**, a voxel-based approach for efficient and accurate neural surface reconstruction. It includes several key designs: the two-stage framework attains a coherent coarse shape and recovers fine details successively; the dual color network helps maintain color-geometry dependency, and the hierarchical geometry feature encourages information propagation across voxels; effective smoothness priors including a gradient smoothness loss further improve the visual quality. Extensive experiments show that Voxurf achieves high efficiency and high quality at the same time.

A EXPERIMENTAL DETAILS

A.1 DATASETS.

The **DTU** (Jensen et al., 2014) dataset contains different static scenes with 49 or 64 posed multi-view images for each scene. It covers a variety of objects with different materials, geometry, and texture. We evaluate our approach on DTU with the same 15 scenes following IDR (Yariv et al., 2020) and quantitatively compare it with previous work on Chamfer Distance, given the ground truth point clouds. The **BlendedMVS** (Yao et al., 2020) dataset contains 113 scenes that cover a variety of real-world environments, providing 31 to 143 posed multi-view images for each. We select 7 challenging scenes following NeuS (Wang et al., 2021) and present qualitative comparisons with previous works.

A.2 IMPLEMENTATION DETAILS

We set the expected number of voxels to be 96^3 at the coarse stage and 256^3 at the fine stage, including an up-scaling step. We use a batch size of 8,192 rays with the point sampling step size on a ray to be half of the voxel size. We train our coarse initialization stage for 10k iterations and the fine geometry optimization stage for 20k iterations with an Adam optimizer. The initial learning rate is set as 1^{-3} for all the MLPs and 0.1 for voxels in the coarse stage, while the SDF voxel starts by 5^{-3} in the fine stage.

We use the same hyper-parameters for all scenes. We use a 3-layer MLP for the coarse training stage and two 4-layer MLPs for the dual color network in the fine training stage. We choose level 2.0 for the hierarchical geometry feature and set the dimension of the learnable feature voxel grid as 6.

For the coarse stage, we set $\lambda_{tv} = 10^{-4}$ and $\lambda_s = 2 \times 10^{-4}$ for the regularization terms and introduce an additional TV term for $V^{(feat)}$ with a weight of 10^{-2} . The Gaussian kernel is 5^3 in size with $\sigma_g = 0.8$. For the fine stage, we set $\lambda_0 = 0.5$ for the reconstruction loss; we set $\lambda_{tv} = 10^{-3}$ and $\lambda_s = 5 \times 10^{-4}$ for the regularization terms. The fine SDF grid starts with a resolution of 160^3 , which is then up-scaled by trilinear interpolation to 256^3 after 15000 iterations.

For the s value in Φ_s in Eqn. 2, we design a function based on the iteration, $s = 1/(i/r + 1/s_{start})$, where s_{start} controls the beginning value of s , i denotes the iteration number, and r basically controls the decaying speed of s along with the increasing iterations. We set $s_{start} = 0.2$, $r = 50$ for the coarse stage and $s_{start} = 0.05$, $r = 50$ for the fine stage.

For all the experimental results on the DTU (Jensen et al., 2014) dataset, our method is trained on the training set with around 90% images for each scene, following (Wang et al., 2021) for the splitting scheme, and the 10% images are used for evaluation of the novel view synthesis task. We notice that the CD performance is only slightly influenced compared to training on the full dataset. For experiments on the BlendedMVS (Yao et al., 2020) dataset, we use all the images for training.

A.3 DETAILS FOR BASELINE METHODS

We include the following baseline methods for comparison: **IDR** (Yariv et al., 2020) reconstructs high-quality surfaces with implicit representation based on foreground object masks and the corresponding mask loss. **NeuS** (Wang et al., 2021) is a state-of-the-art approach that develops a volume rendering method for surface reconstruction, where the mask supervision is optional. Reconstruct-

Table R5: Quantitative evaluation on the DTU dataset for novel view synthesis. Our method outperforms the baselines on all the three metrics.

| Metric | PSNR \uparrow | | | | SSIM \uparrow | | | | LPIPS \downarrow | | | |
|--------|-----------------|--------------|-------|--------------|-----------------|--------------|-------|--------------|--------------------|--------------|-------|--------------|
| | Scan | NeRF | DVGO | NeuS | Ours | NeRF | DVGO | NeuS | Ours | NeRF | DVGO | NeuS |
| 24 | 26.97 | 27.77 | 26.13 | 27.89 | 0.772 | 0.830 | 0.764 | 0.857 | 0.331 | 0.277 | 0.348 | 0.239 |
| 37 | 25.99 | 25.96 | 24.08 | 26.90 | 0.811 | 0.833 | 0.798 | 0.870 | 0.206 | 0.184 | 0.222 | 0.160 |
| 40 | 27.68 | 27.75 | 26.73 | 28.81 | 0.786 | 0.791 | 0.747 | 0.841 | 0.304 | 0.303 | 0.352 | 0.274 |
| 55 | 29.39 | 30.42 | 28.06 | 31.02 | 0.917 | 0.939 | 0.887 | 0.950 | 0.143 | 0.116 | 0.177 | 0.108 |
| 63 | 33.07 | 34.35 | 28.69 | 34.38 | 0.936 | 0.953 | 0.937 | 0.957 | 0.128 | 0.095 | 0.129 | 0.083 |
| 65 | 30.87 | 31.18 | 31.41 | 31.48 | 0.954 | 0.956 | 0.958 | 0.960 | 0.114 | 0.103 | 0.112 | 0.094 |
| 69 | 27.90 | 29.52 | 28.96 | 30.13 | 0.844 | 0.921 | 0.909 | 0.928 | 0.308 | 0.190 | 0.223 | 0.181 |
| 83 | 33.49 | 36.94 | 31.56 | 37.43 | 0.948 | 0.969 | 0.950 | 0.968 | 0.125 | 0.084 | 0.120 | 0.084 |
| 97 | 27.43 | 27.67 | 25.51 | 28.35 | 0.900 | 0.914 | 0.901 | 0.923 | 0.200 | 0.168 | 0.192 | 0.155 |
| 105 | 31.68 | 32.85 | 29.18 | 32.94 | 0.910 | 0.928 | 0.896 | 0.932 | 0.186 | 0.154 | 0.218 | 0.148 |
| 106 | 30.73 | 33.75 | 32.60 | 34.17 | 0.879 | 0.933 | 0.914 | 0.947 | 0.244 | 0.167 | 0.201 | 0.138 |
| 110 | 29.61 | 33.10 | 30.83 | 32.70 | 0.872 | 0.941 | 0.917 | 0.937 | 0.241 | 0.153 | 0.200 | 0.153 |
| 114 | 29.37 | 30.18 | 29.32 | 30.97 | 0.901 | 0.914 | 0.897 | 0.926 | 0.193 | 0.174 | 0.216 | 0.159 |
| 118 | 33.44 | 36.11 | 35.91 | 37.24 | 0.915 | 0.957 | 0.948 | 0.964 | 0.199 | 0.123 | 0.156 | 0.110 |
| 122 | 33.41 | 36.99 | 35.49 | 37.97 | 0.935 | 0.967 | 0.957 | 0.972 | 0.142 | 0.088 | 0.114 | 0.076 |
| mean | 30.07 | 31.64 | 29.63 | 32.16 | 0.885 | 0.916 | 0.892 | 0.929 | 0.204 | 0.159 | 0.199 | 0.144 |

Table R6: Quantitative evaluation on DTU dataset (without mask).

| Scan | 24 | 37 | 40 | 55 | 63 | 65 | 69 | 83 | 97 | 105 | 106 | 110 | 114 | 118 | 122 | mean |
|-----------------------------------|-------------|-------------|-------------|-------------|-------------|-------------|-------------|-------------|-------------|-------------|-------------|-------------|-------------|-------------|-------------|-------------|
| Colmap (Schönberger et al., 2016) | 0.81 | 2.05 | 0.73 | 1.22 | 1.79 | 1.58 | 1.02 | 3.05 | 1.40 | 2.05 | 1.00 | 1.32 | 0.49 | 0.78 | 1.17 | 1.36 |
| NeRF (Mildenhall et al., 2020) | 1.90 | 1.60 | 1.85 | 0.58 | 2.28 | 1.27 | 1.47 | 1.67 | 2.05 | 1.07 | 0.88 | 2.53 | 1.06 | 1.15 | 0.96 | 1.49 |
| UNISURF (Oechsle et al., 2021) | 1.32 | 1.36 | 1.72 | 0.44 | 1.35 | 0.79 | 0.80 | 1.49 | 1.37 | 0.89 | 0.59 | 1.47 | 0.46 | 0.59 | 0.62 | 1.02 |
| VolSDF Yariv et al. (2021) | 1.14 | 1.26 | 0.81 | 0.49 | 1.25 | 0.70 | 0.72 | 1.29 | 1.18 | 0.70 | 0.66 | 1.08 | 0.42 | 0.61 | 0.55 | 0.86 |
| NeuS (Wang et al., 2021) | 1.00 | 1.37 | 0.93 | 0.43 | 1.10 | 0.65 | 0.57 | 1.48 | 1.09 | 0.83 | 0.52 | 1.20 | 0.35 | 0.49 | 0.54 | 0.84 |
| Ours | 0.71 | 0.78 | 0.43 | 0.35 | 1.03 | 0.76 | 0.74 | 1.49 | 1.04 | 0.74 | 0.51 | 1.12 | 0.41 | 0.55 | 0.45 | 0.74 |

tion results for NeuS are implemented with its official code ¹ and the pre-trained models, and the novel view rendering results are provided by the authors. **NeRF** (Mildenhall et al., 2020) first proposes to use the neural radiance field for novel view synthesis. Though not specifically designed for surface reconstruction, we can extract a noise geometry from a trained NeRF model with a selected threshold. In this paper, the reconstruction evaluation results for NeRF are directly taken from (Wang et al., 2021) for a fair comparison, while we also implement NeRF with nerf-pytorch ² for novel view synthesis. **DVGO** (Sun et al., 2021) accelerates NeRF with a hybrid representation. We use the official code ³ and implement DVGO-v2 (Sun et al., 2022) for comparison, which is 2-3 times faster than the DVGO-v1. Similarly, we select a threshold to extract the geometry from the density voxel grid, as to be introduced below. Results for these methods with the aid of foreground object masks are presented in Table 1 of the main text.

We also include several baselines that do not rely on foreground object masks: **Colmap** (Schönberger et al., 2016) is a widely-used classical Multi-view stereo method. **UNISURF** (Oechsle et al., 2021) uses the occupancy field to represent the geometry and improves reconstruction quality by shrinking the sample region of volume rendering during training. **VolSDF** (Yariv et al., 2021) defines the volume density function as Laplace’s cumulative distribution function (CDF) applied to a SDF representation for surface reconstruction. We also compare with **NeRF** (Mildenhall et al., 2020) and **NeuS** (Wang et al., 2021) under the without-mask setting. All the results above are directly adopted from the original papers. Their comparisons to our method under this setting are shown in Table R6.

¹<https://github.com/Totoro97/NeuS>

²<https://github.com/yenchenlin/nerf-pytorch>

³<https://github.com/sunset1995/DirectVoxGO>

Table R7: Ablation over the level selection for hierarchical geometry feature. The performance first increases together with the level and then converges after level 2.0.

| level | 0 | 0.5 | 1 | 1.5 | 2 | 2.5 | 3 |
|-------|------|------|------|------|-------------|------|-------------|
| CD | 0.98 | 0.75 | 0.74 | 0.74 | 0.72 | 0.73 | 0.72 |

Table R8: Ablation over the geometry feature design. It indicates that a combination of both *Gradient* and *SDF* produces the best result.

| CD (mean) | 0.79 | 0.76 | 0.74 | 0.72 |
|-----------|------|------|------|-------------|
| Gradient | | ✓ | | ✓ |
| SDF | | | ✓ | ✓ |

Table R9: Ablation over different smoothness priors. Our gradient smoothness loss is proved effective by this quantitative evaluation.

| CD (mean) | 1.18 | 0.79 | 0.74 | 0.72 |
|--------------------------|------|------|------|-------------|
| SDF TV | | ✓ | | ✓ |
| Gradient smoothness loss | | | ✓ | ✓ |

B ADDITIONAL EXPERIMENTAL RESULTS

B.1 NOVEL VIEW SYNTHESIS.

We report the results for novel view synthesis on the DTU dataset in Table R5. Our method outperforms the baselines in all three metrics, including PSNR, SSIM (Wang et al., 2004), and LPIPS (Zhang et al., 2018) (VGG). Examples of rendered images at testing views are shown in Fig. S10 and Fig. S11 in Sec. C.

B.2 COMPARISONS FOR THE W/O MASK SETTING.

Our method can also work on cases where the background is not clean. Following NeRF++ Zhang et al. (2020) and MipNeRF-360 Barron et al. (2022), we invert the background points outside the unit sphere into the unit sphere by $x' = x/r^2, y' = y/r^2, z' = z/r^2$, where $r = \sqrt{x^2 + y^2 + z^2}$. We then represent the background with another density voxel grid, together with a feature grid and a shallow MLP. We report our results and comparisons to previous approaches in Table R6.

B.3 ADDITIONAL ABLATION STUDIES AND ANALYSIS

Ablation over the hierarchical geometry feature. For hierarchical geometry feature design, we explore different design details, including the level selection and the effect of gradient and SDF value, as shown in Table R7 and Table R8, respectively.

Ablation over smoothness priors. We introduce two regularization terms as smoothness priors during training, *i.e.* the TV on the SDF voxel grid and a gradient smoothness prior. We carry out an ablation study on them during the fine training stage in Table R9, where we reveal the effectiveness of our gradient smoothness loss via quantitative comparisons.

Ablation over the voxel grid resolution. The voxel grid resolution denotes the number of voxels contained in $V^{(sdf)}$ of the fine training stage. We study the effect of voxel grid resolution by keeping all the other settings to be the same, as shown in Table R10. Increasing the voxel grid resolution from 128^3 to 192^3 and from 192^3 to 256^3 consistently results in lower Chamfer Distance (CD) with longer training time. However, the case with 320^3 achieves a similar CD with 256^3 , and requires a higher training cost. Thus, we take the number of voxels to be 256^3 as the default setting in the other experiments.

Two-stage training process. Our method adopts a two-stage training pipeline. We show the curve of Chamfer Distance and the visualization result by the end of each stage in Fig. S8. We show that 1) we can obtain a coherent shape by the end of the Stage-1 (coarse training stage), while the performance is limited by the low resolution that the details are hard to be reconstructed; 2) the fine details are recovered by the end of Stage-2 (fine training stage) and the overall structure is consistent with the coarse shape of Stage-1.

Table R10: The effect of voxel grid resolution on reconstruction performance and training time. All the cases below are trained with the same settings except for the voxel grid resolution.

| Resolution | 128 ³ | 192 ³ | 256 ³ | 320 ³ |
|------------|------------------|------------------|------------------|------------------|
| CD (mean) | 0.79 | 0.75 | 0.72 | 0.73 |
| Train time | 11 mins | 12 mins | 14 mins | 17 mins |

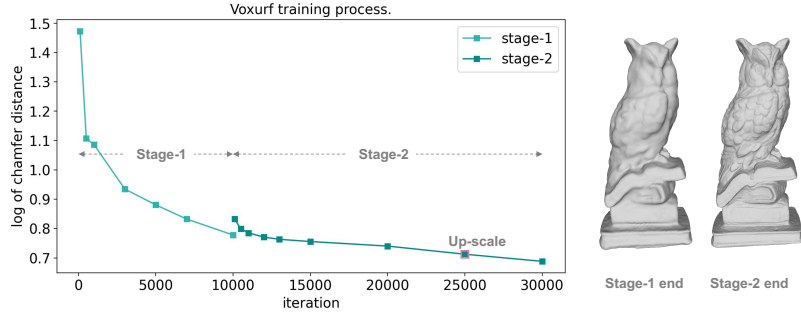


Figure S8: The two-stage training process of Voxurf. The number in the vertical axis is calculated by $\log_{10}(10x)$ for better visualization.

Threshold selection. To extract the surface from a trained DVGO (Sun et al., 2021) model, we can first obtain the alpha value for any point in the 3D space by density interpolation and activation. And then, we show how we select a proper alpha threshold when we extract the surface in Fig. S9. A small threshold like 0.001 and 0.01 usually results in noise areas floating above the surface, while a large one like 0.5 and 0.8 would lead to an incomplete surface with large holes. We thus select 0.1 as the alpha threshold that is adopted in this paper.

C ADDITIONAL QUALITATIVE COMPARISONS

Finally, we show the qualitative comparisons for novel view synthesis in Fig. S10 and Fig. S11, and we show additional surface reconstruction results in Fig S12, Fig S13, and Fig S14.

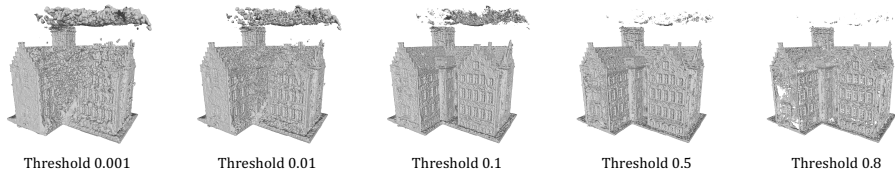


Figure S9: Comparisons of Alpha threshold selection for surface extraction from a trained DVGO (Sun et al., 2021) model. A large threshold leads to holes and the incomplete surface, while a small one leads to floating noises above the surface.



Figure S10: Qualitative comparisons on DTU for novel view synthesis. (Part 1/2)



Figure S11: Qualitative comparisons on DTU for novel view synthesis. (Part 2/2)

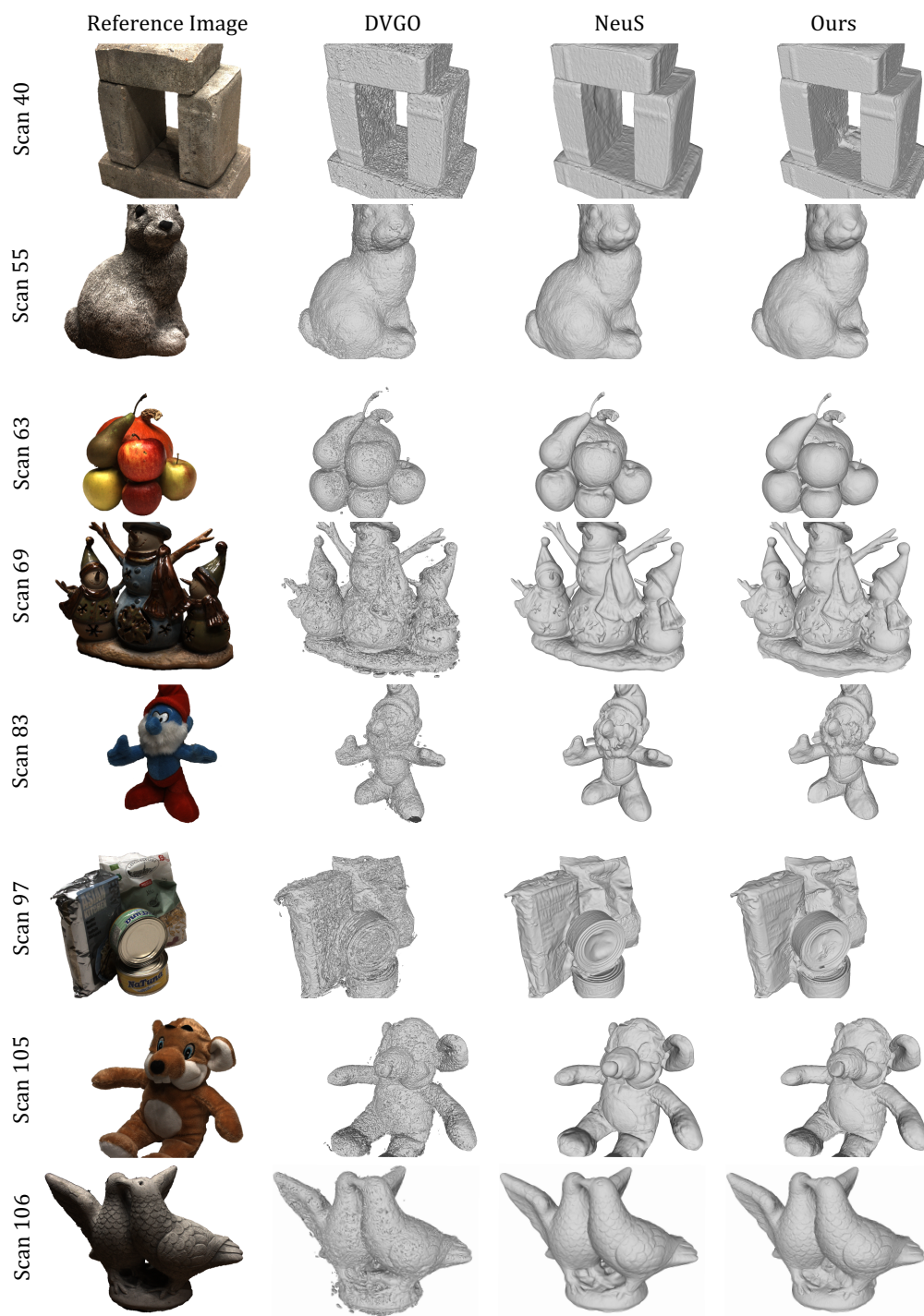


Figure S12: Additional surface reconstruction comparisons on DTU. (Part 1/2)

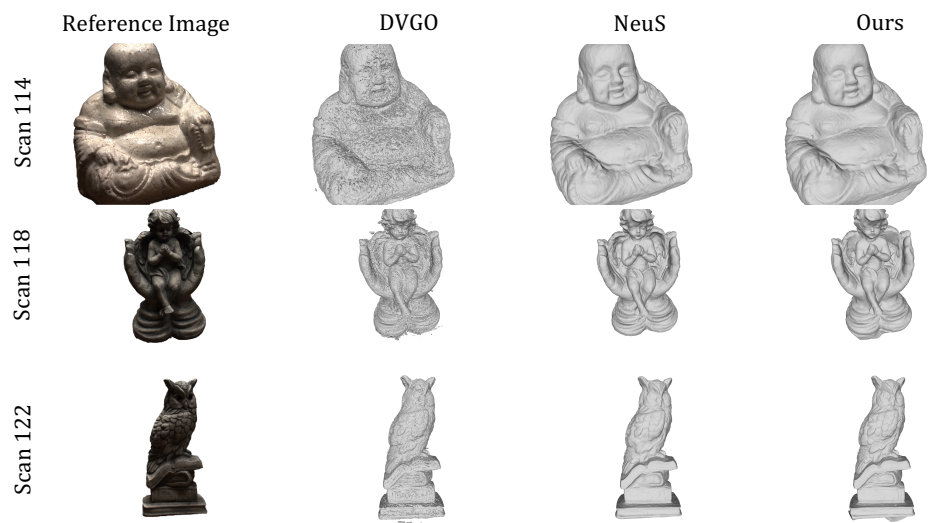


Figure S13: Additional surface reconstruction comparisons on DTU. (Part 2/2)

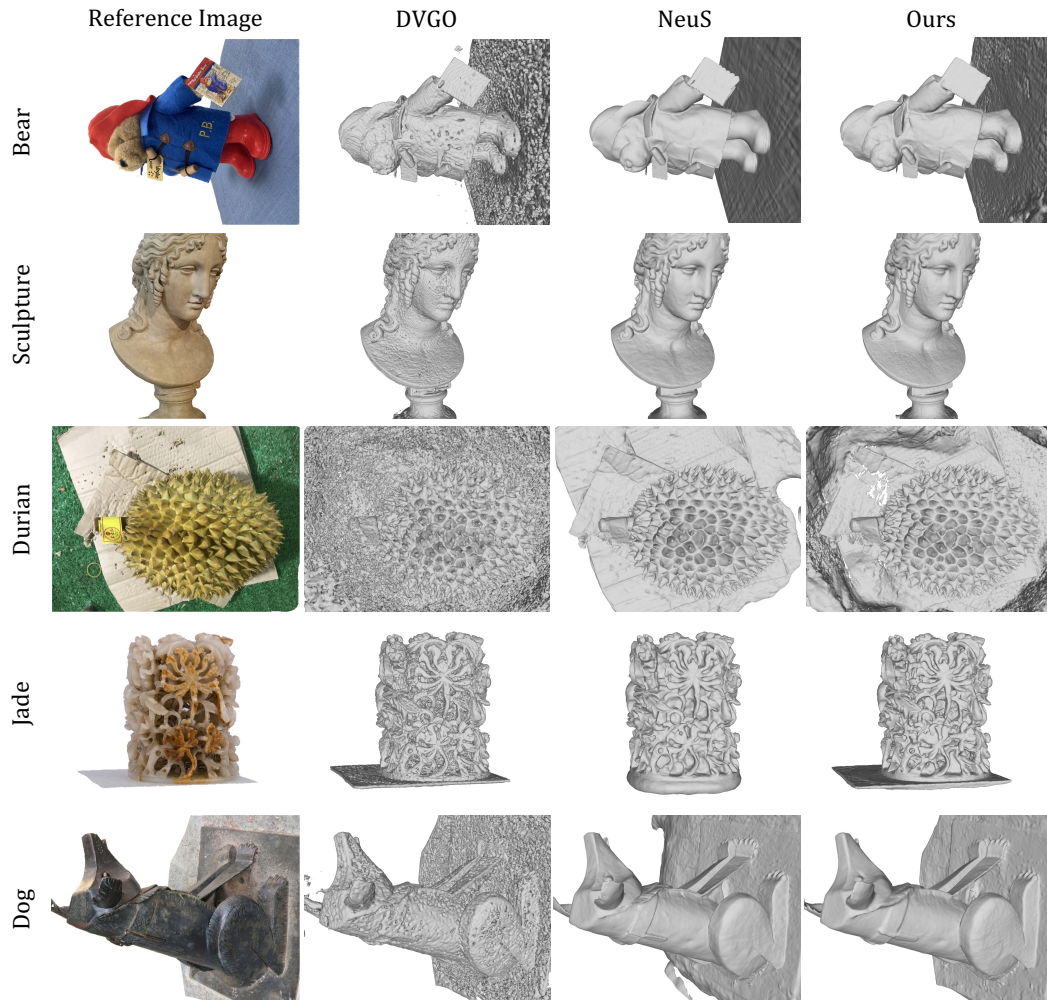


Figure S14: Additional surface reconstruction comparisons on BlendedMVS.

REFERENCES

- Matan Atzmon, Niv Haim, Lior Yariv, Ofer Israelov, Haggai Maron, and Yaron Lipman. Controlling neural level sets. *Advances in Neural Information Processing Systems*, 32, 2019.
- Jonathan T. Barron, Ben Mildenhall, Dor Verbin, Pratul P. Srinivasan, and Peter Hedman. Mip-nerf 360: Unbounded anti-aliased neural radiance fields. *CVPR*, 2022.
- Anpei Chen, Zexiang Xu, Andreas Geiger, Jingyi Yu, and Hao Su. Tensorf: Tensorial radiance fields. In *European Conference on Computer Vision (ECCV)*, 2022.
- Zhiqin Chen and Hao Zhang. Learning implicit fields for generative shape modeling. In *Proceedings of the IEEE/CVF Conference on Computer Vision and Pattern Recognition*, pp. 5939–5948, 2019.
- François Darmon, Bénédicte Bascle, Jean-Clément Devaux, Pascal Monasse, and Mathieu Aubry. Improving neural implicit surfaces geometry with patch warping. 2021. URL <https://arxiv.org/2112.09648>.
- Jiemin Fang, Taoran Yi, Xinggang Wang, Lingxi Xie, Xiaopeng Zhang, Wenyu Liu, Matthias Nießner, and Qi Tian. Fast dynamic radiance fields with time-aware neural voxels. [arxiv:2205.15285](https://arxiv.org/2205.15285), 2022.
- Rasmus Jensen, Anders Dahl, George Vogiatzis, Engin Tola, and Henrik Aanæs. Large scale multi-view stereopsis evaluation. In *Proceedings of the IEEE conference on computer vision and pattern recognition*, pp. 406–413, 2014.
- Yue Jiang, Dantong Ji, Zhizhong Han, and Matthias Zwicker. Sdfdiff: Differentiable rendering of signed distance fields for 3d shape optimization. In *The IEEE/CVF Conference on Computer Vision and Pattern Recognition (CVPR)*, June 2020.
- Petr Kellnhofer, Lars C Jebe, Andrew Jones, Ryan Spicer, Kari Pulli, and Gordon Wetzstein. Neural lumigraph rendering. In *Proceedings of the IEEE/CVF Conference on Computer Vision and Pattern Recognition*, pp. 4287–4297, 2021.
- Shaohui Liu, Yinda Zhang, Songyou Peng, Boxin Shi, Marc Pollefeys, and Zhaopeng Cui. Dist: Rendering deep implicit signed distance function with differentiable sphere tracing. In *Proceedings of the IEEE/CVF Conference on Computer Vision and Pattern Recognition*, pp. 2019–2028, 2020.
- Stephen Lombardi, Tomas Simon, Jason Saragih, Gabriel Schwartz, Andreas Lehrmann, and Yaser Sheikh. Neural volumes: Learning dynamic renderable volumes from images. [arXiv preprint arXiv:1906.07751](https://arxiv.org/1906.07751), 2019.
- Nelson Max. Optical models for direct volume rendering. *IEEE Transactions on Visualization and Computer Graphics*, 1(2):99–108, 1995.
- Lars Mescheder, Michael Oechsle, Michael Niemeyer, Sebastian Nowozin, and Andreas Geiger. Occupancy networks: Learning 3d reconstruction in function space. In *Proceedings of the IEEE/CVF Conference on Computer Vision and Pattern Recognition*, pp. 4460–4470, 2019.
- Ben Mildenhall, Pratul P. Srinivasan, Rodrigo Ortiz-Cayon, Nima Khademi Kalantari, Ravi Ramamoorthi, Ren Ng, and Abhishek Kar. Local light field fusion: Practical view synthesis with prescriptive sampling guidelines. *ACM Transactions on Graphics (TOG)*, 2019.
- Ben Mildenhall, Pratul P Srinivasan, Matthew Tancik, Jonathan T Barron, Ravi Ramamoorthi, and Ren Ng. Nerf: Representing scenes as neural radiance fields for view synthesis. In *European conference on computer vision*, pp. 405–421. Springer, 2020.
- Thomas Müller, Alex Evans, Christoph Schied, and Alexander Keller. Instant neural graphics primitives with a multiresolution hash encoding. *ACM Trans. Graph.*, 2022.
- Michael Niemeyer, Lars Mescheder, Michael Oechsle, and Andreas Geiger. Differentiable volumetric rendering: Learning implicit 3d representations without 3d supervision. In *Proceedings of the IEEE/CVF Conference on Computer Vision and Pattern Recognition*, pp. 3504–3515, 2020.

-
- Michael Oechsle, Songyou Peng, and Andreas Geiger. Unisurf: Unifying neural implicit surfaces and radiance fields for multi-view reconstruction. In Proceedings of the IEEE/CVF International Conference on Computer Vision, pp. 5589–5599, 2021.
- Jeong Joon Park, Peter Florence, Julian Straub, Richard Newcombe, and Steven Lovegrove. Deepsdf: Learning continuous signed distance functions for shape representation. In Proceedings of the IEEE/CVF Conference on Computer Vision and Pattern Recognition, pp. 165–174, 2019.
- Leonid I Rudin and Stanley Osher. Total variation based image restoration with free local constraints. In Proceedings of 1st international conference on image processing, volume 1, pp. 31–35. IEEE, 1994.
- Shunsuke Saito, Zeng Huang, Ryota Natsume, Shigeo Morishima, Angjoo Kanazawa, and Hao Li. Pifu: Pixel-aligned implicit function for high-resolution clothed human digitization. In Proceedings of the IEEE/CVF International Conference on Computer Vision, pp. 2304–2314, 2019.
- Johannes L Schönberger, Enliang Zheng, Jan-Michael Frahm, and Marc Pollefeys. Pixelwise view selection for unstructured multi-view stereo. In European Conference on Computer Vision, pp. 501–518. Springer, 2016.
- Vincent Sitzmann, Michael Zollhöfer, and Gordon Wetzstein. Scene representation networks: Continuous 3d-structure-aware neural scene representations. In Advances in Neural Information Processing Systems, 2019.
- Cheng Sun, Min Sun, and Hwann-Tzong Chen. Direct voxel grid optimization: Super-fast convergence for radiance fields reconstruction. arXiv preprint arXiv:2111.11215, 2021.
- Cheng Sun, Min Sun, and Hwann-Tzong Chen. Improved direct voxel grid optimization for radiance fields reconstruction, 2022.
- Matthew Tancik, Pratul Srinivasan, Ben Mildenhall, Sara Fridovich-Keil, Nithin Raghavan, Utkarsh Singhal, Ravi Ramamoorthi, Jonathan Barron, and Ren Ng. Fourier features let networks learn high frequency functions in low dimensional domains. Advances in Neural Information Processing Systems, 33:7537–7547, 2020.
- Briac Toussaint, Maxime Genisson, and Jean-Sébastien Franco. Fast Gradient Descent for Surface Capture Via Differentiable Rendering. In 3DV 2022 - International Conference on 3D Vision, pp. 1–10, September 2022.
- Jingwen Wang, Tymoteusz Bleja, and Lourdes Agapito. Go-surf: Neural feature grid optimization for fast, high-fidelity rgb-d surface reconstruction. In 2022 International Conference on 3D Vision (3DV). IEEE, 2022.
- Peng Wang, Lingjie Liu, Yuan Liu, Christian Theobalt, Taku Komura, and Wenping Wang. Neus: Learning neural implicit surfaces by volume rendering for multi-view reconstruction. NeurIPS, 2021.
- Zhou Wang, Alan C Bovik, Hamid R Sheikh, and Eero P Simoncelli. Image quality assessment: from error visibility to structural similarity. IEEE transactions on image processing, 13(4):600–612, 2004.
- Suttisak Wizadwongsa, Pakkapon Phongthawee, Jiraphon Yenphraphai, and Supasorn Suwanakorn. Nex: Real-time view synthesis with neural basis expansion. In Proceedings of the IEEE/CVF Conference on Computer Vision and Pattern Recognition, pp. 8534–8543, 2021.
- Qiangeng Xu, Zexiang Xu, Julien Philip, Sai Bi, Zhixin Shu, Kalyan Sunkavalli, and Ulrich Neumann. Point-nerf: Point-based neural radiance fields. arXiv preprint arXiv:2201.08845, 2022.
- Yao Yao, Zixin Luo, Shiwei Li, Jingyang Zhang, Yufan Ren, Lei Zhou, Tian Fang, and Long Quan. Blendedmvs: A large-scale dataset for generalized multi-view stereo networks. In Proceedings of the IEEE/CVF Conference on Computer Vision and Pattern Recognition, pp. 1790–1799, 2020.

-
- Lior Yariv, Yoni Kasten, Dror Moran, Meirav Galun, Matan Atzmon, Basri Ronen, and Yaron Lipman. Multiview neural surface reconstruction by disentangling geometry and appearance. Advances in Neural Information Processing Systems, 33, 2020.
- Lior Yariv, Jiatao Gu, Yoni Kasten, and Yaron Lipman. Volume rendering of neural implicit surfaces. In Thirty-Fifth Conference on Neural Information Processing Systems, 2021.
- Alex Yu, Sara Fridovich-Keil, Matthew Tancik, Qinhong Chen, Benjamin Recht, and Angjoo Kanazawa. Plenoxels: Radiance fields without neural networks. arXiv preprint arXiv:2112.05131, 2021.
- Jingyang Zhang, Yao Yao, and Long Quan. Learning signed distance field for multi-view surface reconstruction. International Conference on Computer Vision (ICCV), 2021.
- Kai Zhang, Gernot Riegler, Noah Snavely, and Vladlen Koltun. Nerf++: Analyzing and improving neural radiance fields. arXiv preprint arXiv:2010.07492, 2020.
- Richard Zhang, Phillip Isola, Alexei A Efros, Eli Shechtman, and Oliver Wang. The unreasonable effectiveness of deep features as a perceptual metric. In Proceedings of the IEEE conference on computer vision and pattern recognition, pp. 586–595, 2018.